Article

A Fe-NC electrocatalyst boosted by trace bromide ions with high performance in proton exchange membrane fuel cells

Check for updates

Shuhu Yin[1,6], Long Chen[1,6], Jian Yang[2,6], Xiaoyang Cheng[1], Hongbin Zeng [1], Yuhao Hong[3], Huan Huang[4], Xiaoxiao Kuai[1,3], Yangu Lin [5], Rui Huang [1] ✉, Yanxia Jiang [1] ✉ & Shigang Sun [1] ✉

Replacement of expensive and rare platinum with metal−nitrogen−carbon catalysts for oxygen reduction reactions in proton exchange membrane fuel cells is hindered by their inferior activity. Herein, we report a highly active iron-nitrogen-carbon catalyst by optimizing the carbon structure and coordination environments of Fe-N_4 sites. A critical high-temperature treatment with ammonium chloride and ammonium bromide not only enhances the intrinsic activity and density of Fe-N_4 sites, but also introduces numerous defects, trace Br ions and creates mesopores in the carbon framework. Notably, surface Br ions significantly improve the interaction between the ionomer and catalyst particles, promoting ionomer infiltration and optimizing the O_2 transport and charge transfer at triple-phase boundary. This catalyst delivers a high peak power density of 1.86 W cm^{-2} and 54 mA cm^{-2} at 0.9 $V_{iR-free}$ in a H_2-O_2 fuel cells at 80 °C. Our findings highlight the critical role of interface microenvironment regulation.

Proton exchange membrane fuel cells (PEMFCs), as zero-emission power generation systems, are highly desirable for a variety of applications due to their environmental friendliness[1–3]. Achieving mass production and commercialization of PEMFCs is heavily contingent on their cost competitiveness[4–8]. Currently, the utilization of Pt-based catalysts remains inevitable, accounting for 41% of the total stack costs. Approximately 80% of the total Pt loading at is required for the PEMFCs cathode due to the sluggish kinetics of the oxygen reduction reaction (ORR)[9–12]. The development of PGM-free ORR catalysts to replace Pt has been pursued for over a decade[13]. The US Department of Energy (DOE) has set ambitious target for PGM-free catalysts; for instance, they have targeted a current density of 44 mA cm^{-2} at absolute 150 kPa H_2–O_2 and 0.9 $V_{iR-free}$ (where

iR-free indicates that the internal resistance is compensated for) by 2025[14].

The M−NC catalysts, where M is a transition metal such as Fe and Co, have demonstrated encouraging activity levels[15–21]. The nitrogen-doped carbon matrix (NC) is able to stabilize metal ions, such as Fe, through the formation of Fe−N_x coordination with its nitrogen ligands[22–24]. This coordination is strikingly similar to the metal-N_4 core found in metal porphyrins and phthalocyanines. Significant advancements have been achieved recently, especially with Fe−NC, to improve the acidic ORR activity of M−NC materials[25–31]. However, their activity and stability levels, remain well below the necessary performance standards required to replace PGM catalysts at the cathode, underscoring the significance of further improving activity. Numerous

[1]State Key Laboratory of Physical Chemistry of Solid Surfaces, Engineering Research Center of Electrochemical Technologies of Ministry of Education, College of Chemistry and Chemical Engineering, and Discipline of Intelligent Instrument and Equipment, Xiamen University, Xiamen, P. R. China. [2]Center of Advanced Electrochemical Energy, Institute of Advanced Interdisciplinary Studies, School of Chemistry and Chemical Engineering, Chongqing University, Chongqing, P.R. China. [3]Fujian Science & Technology Innovation Laboratory for Energy Materials of China (Tan Kah Kee Innovation Laboratory), Xiamen, Fujian, China. [4]Beijing Synchrotron Radiation Facility, Institute of High Energy Physics, Chinese Academy of Sciences, Beijing, P. R. China. [5]National Synchrotron Radiation Research Center, Hsinchu, Taiwan, R.O.C. [6]These authors contributed equally: Shuhu Yin, Long Chen, Jian Yang. ✉ e-mail: rhuang@xmu.edu.cn; yxjiang@xmu.edu.cn; sgsun@xmu.edu.cn

synthesis techniques have been used in an attempt to fine-tune the Fe−NC structures in order to increase the ORR activity. The primary objective is to enhance their intrinsic activity and optimize the amount of atomically distributed iron as Fe−N$_x$[28]. Only patchy success has been seen thus far, with the majority of documented Fe−NC reaching atomically scattered iron concentrations of 0.5 to 2.0 wt%[32]. Higher Fe content causes partial or total Fe clustering during pyrolysis, resulting in the formation of metallic nanoparticles, iron carbide, iron nitride, and other compounds[33]. Studies have shown that single-atom Fe loading may be increased by up to 7.0 wt%[28,34,35]. When these Fe−NC catalysts are tuned, they exhibit half-wave potentials similar to those of Pt measured at the rotating disk electrode (RDE)[27]. More significantly, their fuel cell current densities, which stand at 41.3 mA cm^{-2} at 0.9 V$_{iR-free}$, have reached previously unheard-of heights[28]. Though significant advancements in Fe−NC catalysts have been made, the DOE 2025 target for PGM-free catalysts has not yet been met. For this purpose, it is necessary to further improve the intrinsic activity and active site density of Fe−NC catalysts. In addition, the reaction environment under the operating conditions of PEMFCs also needs to be regulated by special strategies.

Here, we developed a Fe−NC electrocatalyst with trace Br ion distribution, which exhibited excellent fuel cell performance. NH$_4$X (X = Cl, Br) salts were added to the pyrolysis process, and decomposed to produce the gases such as NH$_3$, HCl, and HBr. These gases not only etched the carbon substrate to form more carbon defects and mesopores, but also successfully distributed trace Br ions evenly on the surface of the Fe−NC catalyst. Based on the subsequent characterization results, the intrinsic activity and site density of the prepared Fe−NC^{BrCl} catalyst were improved. Interestingly, the trace Br ions distributed on the surface promoted the uniform distribution of the ionomers on the surface of the catalyst particles, and even penetrated into the interior of the particles. Benefitting from the smooth mass transfer and faster interfacial electron transfer in the catalytic layer of Fe−NC^{BrCl} cathode, the constructed Fe−NC^{BrCl} catalyst reached a high peak power density of 1.86 W cm^{-2}. And the current density of 54 mA cm^{-2} at 0.9 V$_{iR-free}$ was attained following the DOE test protocol, exceeding the DOE 2025 target (44 mA cm^{-2} at 0.9 V$_{iR-free}$).

Results

Catalyst synthesis and structures

Supplementary Fig. 1 describes the two-stage strategy for the synthesis of highly active Fe−N−C catalysts. Initially, a ZIF-8@Phen composite precursor was thermally activated to form NC carriers and the micropores in the carriers accounted for more than 90% of NC carriers (Supplementary Figs. 2 and 3, Table 1). The Fe−NC catalyst was then treated at 900 °C in an Ar atmosphere with ammonium chloride and ammonium bromide salt (NH$_4$Cl and NH$_4$Br, named BrCl), and the final catalyst was named as Fe−NC^{BrCl} (Supplementary Fig. 4). Mesopores and abundant carbon defects emerged during the BrCl treatment due to the etching effect of HCl, HBr, and NH$_3$, which are the decomposition products of NH$_4$Cl and NH$_4$Br (Supplementary Figs. 5−7, Supplementary Movie 1). Figure 1a demonstrated the well-dispersed atomic Fe sites (bright dots) and some holes within the Fe−NC^{BrCl} catalyst via an aberration-corrected high-angle annular dark-field scanning transmission electron microscopy (HAADF-STEM) image. The broad distribution of Fe, N and Br was further demonstrated by the energy-dispersive X-ray spectroscopy (EDS) elemental mapping and XRD (Fig. 1b, c and Supplementary Fig. 8). Figure 1d, e indicated that BrCl treatment can change the N structure and cause the production of pyridine N based on X-ray absorption near edge spectroscopy (XANES) obtained for the N K-edge and X-ray photoelectron spectroscopy (XPS) N 1s spectrum. The formation of additional edge sites is facilitated by the etching effect of NH$_3$, which is generated from the decomposition of NH$_4$X, thereby promoting the incorporation of pyridinic N (Supplementary Fig. 9)[36]. In addition, as demonstrated by the hysteresis

curve, BrCl treatment inhibited the creation of superparamagnetic iron species (Fe derivative clusters) and increased the number of Fe−N$_x$ sites (Fig. 1f, Supplementary Figs. 10 and 11). Fe K-edge energies in X-ray spectra of Fe−NC and Fe−NC^{BrCl} were compared to ferrous and ferric standards including FePc and Fe$_2$O$_3$. The results revealed that Fe was mostly in the Fe^{3+} oxidation state in Fe−NC catalysts, whereas Fe in Fe−NC^{BrCl} had a lower oxidation state (Fig. 1g). A first coordination shell consisting of four nitrogen atoms can faithfully duplicate the Fourier transform of the extended X-ray absorption fine structure (EXAFS) of Fe−NC and Fe−NC^{BrCl} (Fig. 1h, i, Supplementary Table 2). The Fe−N bond length in Fe−NC^{Br} and Fe−NC^{BrCl} treated with NH$_4$Br was expanded relative to that in Fe−NC. NH$_4$Cl and NH$_4$Br played distinct roles in the synthesis of catalysts and reaction mechanisms. NH$_4$Cl was especially effective in fostering the development of mesopores and carbon defects, which were vital for improving mass transport in fuel cells and providing doping sites for Br. In contrast, NH$_4$Br, while less efficient at creating mesopores and carbon defects than NH$_4$Cl, benefits from its ability to decompose into bromine more readily, as HBr yielded Br$_2$ with relative ease (Supplementary Note 1, Figs. 12−14, and Tables 3, 4 for details). When a Br atom was doped adjacent to the Fe−N$_4$ site, its larger atomic radius induced spatial distortion in the Fe−N$_4$ plane, resulting in the elongation of the Fe−N bond (Supplementary Fig. 15 and Table 5). Furthermore, high-sensitivity low-energy ion scattering spectroscopy (HS-LEIS) results revealed that 92% of the Br ions were confined to the surface region (less than 1 nm) of the Fe−NC^{BrCl} particles, with a surface bromine content of 1.51 wt% and a bulk bromine content of 0.12 wt% (Supplementary Figs. 16−18 and Table 6).

ORR activity, SD and TOF in RDE

ORR activity of different Fe−NCs was assessed in a 0.1 M H$_2$SO$_4$ electrolyte by rotating disk electrode (RDE, Supplementary Fig. 19). ORR voltammetry exhibits a strong ORR performance illustrated in Fig. 2a in the order of Fe−NC^{BrCl} > Fe−NC^{Br} ≈ Fe−NC^{Cl} > Fe−NC. With a half-wave potential ($E_{1/2}$) of 0.838 V$_{RHE}$ and a mass activity of 4.302 A g^{-1} at 0.85 V$_{RHE}$, the best performing Fe−NC^{BrCl} catalyst demonstrated high activity. These values are significantly higher than that of the Fe−NC (Fig. 2b). An in-situ nitrite stripping technique was used to assess how catalyst activation affected site activity and site density (SD)[37]. The SD values of Fe−NC was 5.74×10^{19} sites g^{-1} (0.05 sites nm^{-2}), lower than that of the Fe−NC^{BrCl} (6.31×10^{19} sites g^{-1}, 0.06 sites nm^{-2}), which reflects the importance of NH$_4$Cl and NH$_4$Br during pyrolysis (Fig. 2c, Supplementary Figs. 20, 21, Table 7). Furthermore, the SD values of Fe−NC^{BrCl} showed a remarkable degree of agreement with the edge iron site count ($6 \pm 2 \times 10^{19}$ sites g^{-1}) calculated for this catalyst using a domain size of $L_a = 7.3 \pm 2.3$ nm acquired from Anthony et al.[28]. The TOFs on nitrite poisoning were calculated by dividing the reduction in ORR kinetic current by SD. Fe−NC^{BrCl} at 0.80 and 0.85 V$_{RHE}$ had computed TOF values of 4.18 and 0.90 e site^{-1} s^{-1}, respectively, which were higher than Fe−NC (Fig. 2d). This suggests that doping Br atoms increased the TOF of the electrochemically accessible Fe sites[38]. The results from density functional theory (DFT) calculations substantiate that Fe−N$_4$ sites doped with halogen atoms, such as Cl and Br, exhibit an enhanced ability to activate O$_2$ molecules. Nonetheless, the formation of Cl doping is hindered during pyrolysis due to the recalcitrance of HCl. Consequently, Br$_2$, which arises from the decomposition of HBr, is more readily incorporated into Fe−N−C materials[36] (Supplementary Note 2, Figs. 22−26, Table 8).

Performance characterization in a fuel cell

Fe−NC and Fe−NC^{BrCl} served as the cathode catalysts in single-cell PEMFCs tests. Fe−NC^{BrCl} exhibited superior performance under 250 kPa$_{abs}$ H$_2$-O$_2$ conditions, reaching a peak power density (P_{max}) of 1.86 W cm^{-2} at 0.45 V. This value is approximately 0.6 W cm^{-2} higher than that of Fe−NC (Fig. 3a), which exceeded the commercial Pt/C prepared under the same conditions (0.2 mg$_{Pt}$ cm^{-2}, 150 kPa absolute
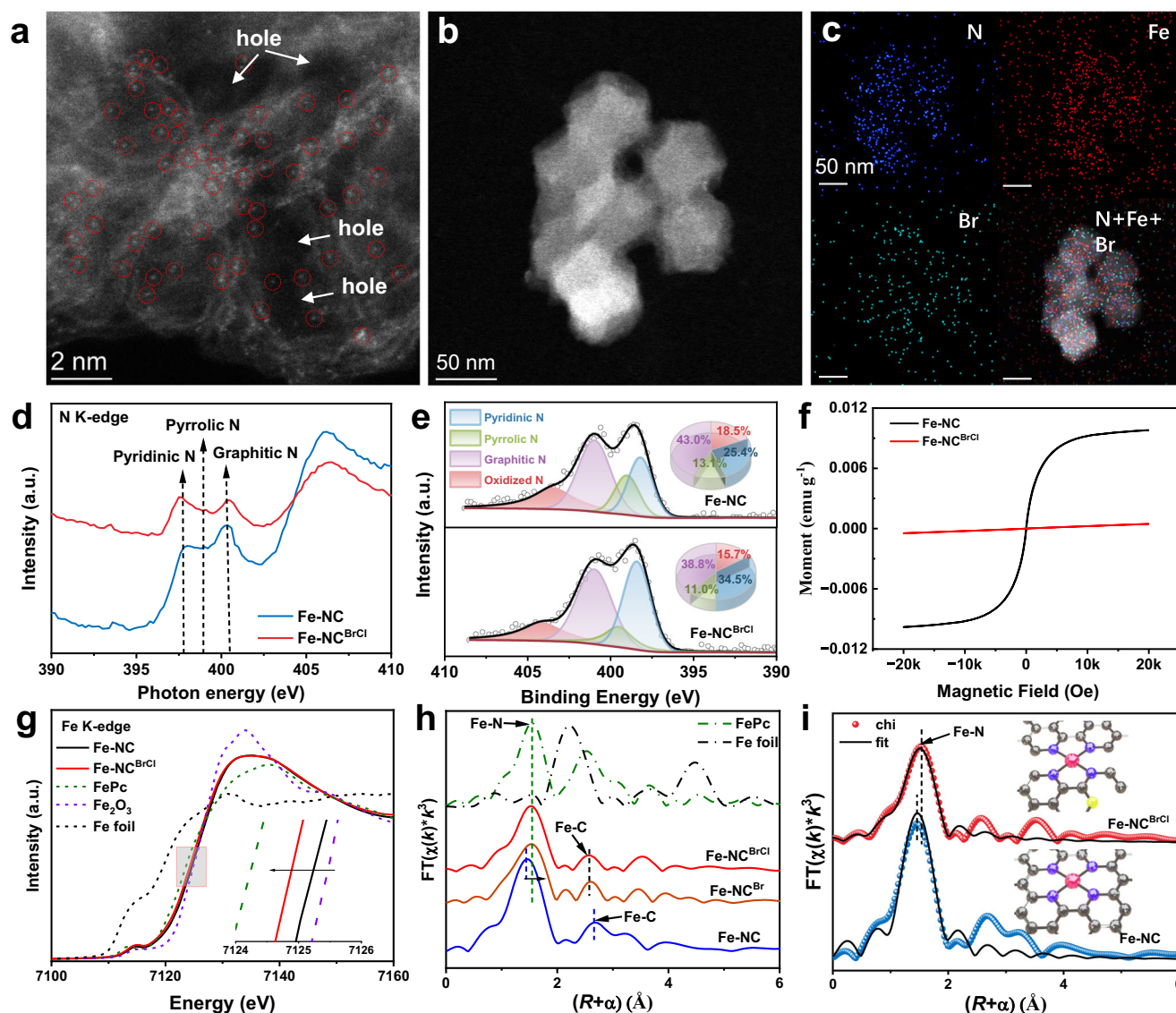
Fig. 1 | Structure analysis of Fe−NC and Fe−NC^{BrCl} catalysts. a Aberration-corrected atomic resolution HAADF-STEM micrograph of Fe−NC^{BrCl}. **b, c** HAADF-STEM images and corresponding EDS mapping. **d** XAS spectra collected at N K-edge. **e** The deconvoluted high-resolution N 1s XPS. **f** The hysteresis curves. **g** Normalized Fe K-edge XANES spectra. **h** Fourier transform of k^3-weighted EXAFS spectra. **i** FT-EXAFS fitting curve, gray ball represents C atom, blue ball represents N atom, red ball represents Fe atom, yellow ball represents Br atom.

O_2 pressure). Fe−NC^{BrCl} cathode has achieved the highest values reported for PGM-free catalysts in recent years (Supplementary Fig. 27 and Table 9)[29,32,39–43]. At 0.8 and 0.7 $V_{iR-free}$, the current densities of Fe−NC^{BrCl} were 0.781 and 3.111 A cm^{-2}, respectively (Fig. 3b, c), surpassing the value achieved by Fe−NC (0.147 and 0.826 A cm^{-2} at 0.8 and 0.7 $V_{iR-free}$). Figure 3d showed that the Tafel slope of Fe−NC^{BrCl} was 84 mV dec^{-1}, which was lower than that of Fe−NC (97 mV dec^{-1}), reflecting the enhanced kinetic activity.

The superior activity of Fe−NC^{BrCl} was further proven in the evaluation of PGM-free catalysts based on the DOE test protocol. As seen in Fig. 4a, Fe−NC^{BrCl} demonstrated a P_{max} of 1.29 W cm^{-2} at 0.45 V. Repeated tests demonstrated excellent repeatability of the high performance (Supplementary Fig. 28). Fe−NC, on the other hand, had a lower P_{max} of 0.97 W cm^{-2}. And for Fe−NC^{BrCl}, the current density at 0.9 $V_{iR-free}$ was 54 mA cm^{-2}, exceeding the DOE 2025 target of 44 mA cm^{-2} at 0.9 $V_{iR-free}$ (Fig. 4b, Supplementary Fig. 29, Table 10). In the H$_2$−air operation (Fig. 4c), Fe−NC^{BrCl} exhibited a P_{max} of 0.88 W cm^{-2}, which was considerably higher than most of the previously reported PGM-free catalysts (Supplementary Table 11). In addition, a measured

current density of 259 mA cm^{-2} and 300 mA cm^{-2} was reached at 0.8 and 0.78 V (or 300 mA cm^{-2} at 0.8 $V_{iR-free}$), only 41 mA cm^{-2} (or 0.02 V) lower than the DOE 2025 target (300 mA cm^{-2} at 0.8 V) (Fig. 4d). In order to better evaluate the practical application performance of Fe−NC^{BrCl}, a three-piece PEMFCs stack with a MEA area of 25 cm^2 was assembled (Supplementary Figs. 30 and 31). To mitigate mass transport limitations at high current densities, which were critical in practical situations involving lower O_2 stoichiometry operation, the Fe−NC^{BrCl} loading in the catalyst layer was set at 2.0 mg cm^{-2}. The polarization curves of stack were acquired in an O_2 atmosphere without background pressure. At 1.8 and 1.4 V (without iR-correction), the PEMFCs stack demonstrated a power of 25.3 and 36.2 W, respectively (Supplementary Fig. 32). It meant that the Fe−NC^{BrCl} catalyst showed promise for practical applications, suggesting the feasibility of widespread application.

Mechanistic insights into the PEMFCs activity enhancement
Within the cathode catalyst layer, the spatial distribution of Fe sites and ionomer was verified by time-of-flight secondary ion mass
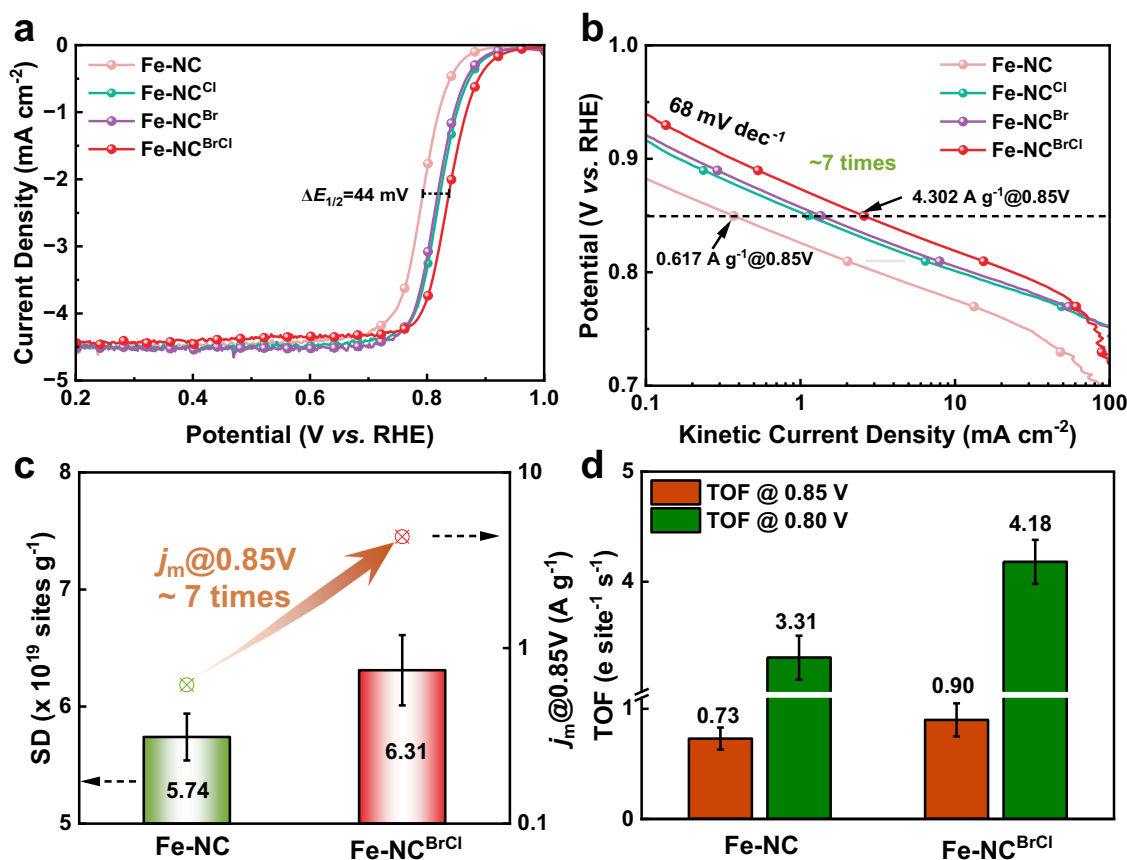
Fig. 2 | ORR activity, SD and TOF measurements of Fe–NCs. a RDE ORR curves measured in O_2-saturated 0.1 M H_2SO_4 at 10 mV s^{-1} with a rotation speed of 900 rpm. The catalyst loading was 0.6 mg cm^{-2}. **b** The kinetic ORR activities of Fe–NCs. **c** Comparison of SD values determined by nitrite stripping method for Fe–NC and Fe–NC^{BrCl} catalysts. **d** Comparison of TOF at 0.80 and 0.85 V_{RHE} for Fe–NC and Fe–NC^{BrCl} catalysts. Error bars represent the standard deviation for three separate measurements.

spectrometry (ToF-SIMS). Two-dimensional images of spatial arrangement of the components on the catalytic layer surfaces corresponding to Fe–NC and Fe–NC^{BrCl} were shown in Fig. 5a, b. S$^-$ ions (green region) indicated sulfonic groups on ionomers, whereas Fe$^+$ ions (red region) indicated Fe sites on Fe–NCs catalysts. It was evident that the thicker ionomer coating on the Fe–NC surface resulted in a sparse dispersion of Fe$^+$ (Fig. 5a). On the surface of the Fe–NC^{BrCl} catalytic layer, trace amounts Br$^-$ ions can be detected (Supplementary Fig. 33). The Br$^-$ ions in Fe–NC^{BrCl} repelled the sulfonic groups of the ionomer, causing a more even dispersion of the ionomer throughout the surface of the catalytic layer (Fig. 5b). The distribution of ionomers in the pores was further investigated by examining the depth distribution curves of Fe$^+$ and SO$_3^-$ ions. The ionomer polymer was typically 2–5 nm in size, too tiny to penetrate the core of the particles and could only be coated on their surface[44,45]. The pores on the surface of Fe–NC particles were mostly micropores, accounting for about 92.8% (Supplementary Table 1). Within the Fe–NC particles, the SO$_3^-$ distribution intensity was essentially nonexistent (Fig. 5c). Nevertheless, Fe–NC^{BrCl} particles formed mesopores as a result of NH_4Cl and NH_4Br breaking down, and the surface Br$^-$ ions on the particles aid in the uniform dispersion of ionomers. Consequently, mesopores allowed a little quantity of ionomers to enter the particles. As a result, the SO$_3^-$ intensity distribution of Fe–NC^{BrCl} particles was also found inside of it (Fig. 5c). Upon analyzing the quantitative correlation between the surface Br content and the P_{max}, a parabolic relationship was observed. The P_{max} attained its apex at an equimolar ratio of NH_4Br to NH_4Cl (1:1) (Supplementary Note 3, Figs. 34–36, Table 12).

By using the limiting current method[46,47], the oxygen transport behavior of membrane electrodes was typically studied (Supplementary Fig. 37). Traditionally, R_{total} was the total of the pressure-dependent transfer impedance R_p and the pressure-independent transfer impedance R_{np}[48]. The oxygen molecules diffusing through the mesopores in the gas diffusion layer (GDL) and the cathode catalytic layer (CCL) were the primary source of the resistance of oxygen diffusion, or R_p. On the other hand, oxygen was transported in the micropores of the catalyst aggregate and the ionomer layer, which caused the resistance to oxygen diffusion, or R_{np}[49–51]. R_{np} somewhat increased as a result of the ionomer seeping into the interior of Fe–NC^{BrCl} particles (Fig. 5d). Lower R_p will arise from improved oxygen transport in the catalytic layer due to the mesoporous Fe–NC^{BrCl}. It was established that the oxygen transport limitation in CCL was predominantly caused by the diffusion resistance of O_2 in the mesopores of the thick cathode catalytic layer, when comparing R_p and R_{np}. The effect of cell temperature on the charge transfer of Fe–NC and Fe–NC^{BrCl} was also examined. As the temperature rose, the high-frequency limit shifted on the real axis in a negative direction (Supplementary Fig. 38). It indicated that the ohmic resistance, that is, the resistance of the membrane, decreased as the temperature of the cell increased. The charge-transfer mechanism was responsible for the depressed ellipse that was seen in all charts in the high-frequency range. The charge transfer resistance R_{ct} was estimated by fitting these impedance measurements to the equivalent circuit (Supplementary Table 13). By replacing the constant phase angle element (CPE) with the double layer capacitance of the Randles equivalent circuit, this
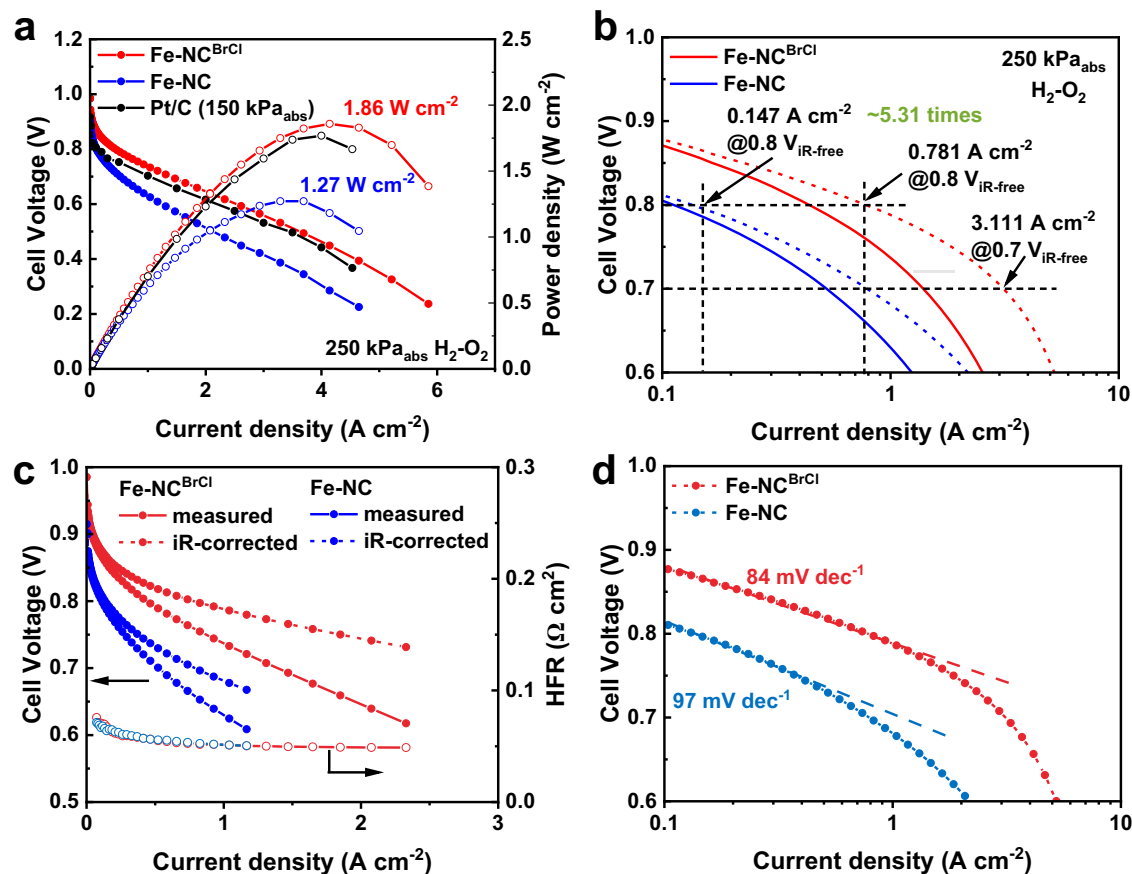
Fig. 3 | Performance tests with Fe−NC and Fe−NC^{BrCl} as the cathode catalysts in a single-cell PEMFCs. a H$_2$-O$_2$ PEMFCs polarization curves. Cathode, ~3.5 mg$_{cat}$ cm^{-2} for Fe−NC and 0.2 mg$_{Pt}$ cm^{-2} for Pt/C; anode, 0.4 mg$_{Pt}$ cm^{-2} Pt/C; GORE-SELECT® membrane (15 μm thickness); 0.3 L H$_2$ min^{-1} and 0.4 L O$_2$ min^{-1} feed, 100% relative humidity (RH), 250 kPa absolute partial pressure H$_2$ and O$_2$, 80 °C, electrode area 1.21 cm^2. The cell voltage and power density are not iR corrected. **b** The polarization curves without (solid line) and with (dotted line) iR-correction and HFR under 250 kPa$_{abs}$ H$_2$-O$_2$ PEMFCs. **c** Current densities at 0.8 V$_{iR-free}$ and 0.7 V$_{iR-free}$. **d** Tafel plots derived from the ORR polarization curves displayed in (**c**).

equivalent circuit was created. A porous electrode causes a depressed semicircle, which is frequently described by the CPE. The exchange current i_0 was calculated from R_{ct} according to the Eq. (1)[52]:

$$i_0 = \left(\frac{RT}{nF}\right)\frac{1}{R_{ct}} \tag{1}$$

The temperature dependency of i_0 might be assessed. In Supplementary Fig. 39, the Arrhenius plot of i_0 was displayed[52]. In addition, good linearity was noted. For Fe−NC^{BrCl}, the apparent activation energy (E_a) of charge transfer was determined to be 8.56 kJ mol^{-1} based on the angle of the plot (Fig. 5e). Compared to the value of 10.56 kJ mol^{-1} for Fe−NC, this value showed a faster charge transfer for Fe−NC^{BrCl}, which was compatible with the lower Tafel slope and lower resistivity (Supplementary Fig. 40). Electrochemical impedance spectroscopy Nyquist plots at 1.0 A cm^{-2} and a Randles model simulation in Fig. 5f further supported the quicker mass and charge transfer. As a result of a richer triple-phase boundary (TPB), faster interfacial charge transfer, better combination of ionomers and Fe active sites, and a more porous catalytic layer, fuel cells assembled with Fe−NC^{BrCl} demonstrated an extremely high levels of operational performance.

Discussion

In summary, we demonstrated a highly active Fe−NC catalyst by adjusting the structure of the carbon carrier and the chemical environment of the active center, representing a critical step towards replacing Pt and enabling large-scale applications of PEMFCs. We explored how the intrinsic activity and site density of Fe−N$_4$ sites in the catalyst can be dramatically enhanced by regulating the catalyst's local carbon structure. The pyrolysis treatment with NH$_4$Cl and NH$_4$Br was essential in creating a high density of carbon defects, mesopores, and trace Br doping on the catalyst surface, which significantly boosted ORR activity of Fe−NC catalyst. A broader dispersion of the ionomer across the surface of catalytic layer was achieved by the Br$^-$ ions on the surface of Fe−NC^{BrCl}, which repelled the sulfonic groups of the ionomer. This resulted in a richer TPB, faster O$_2$ transport, proton transport, and interface charge transfer channels. Thus, the performance of the synthesized Fe−NC^{BrCl} catalyst outperformed the DOE 2025 target, achieving a high peak power density (1.86 and 0.88 W cm^{-2} in O$_2$ and air environment, respectively) and 54 mA cm^{-2} at 0.9 V$_{iR-free}$. Furthermore, employing H$_2$−air, a measured current density of 259 mA cm^{-2} (300 mA cm^{-2} at 0.8 V$_{iR-free}$) was attained at 0.8 V, which is just 41 mA cm^{-2} less than the DOE 2025 target (300 mA cm^{-2} at 0.8 V). In light of this, the achievement of promising activity of a single PGM-free catalyst described here which is equivalent to that of Pt catalysts showed tremendous promise for Pt catalyst replacement in PEMFCs and, eventually, for overcoming the cost barrier of existing PEMFCs.

Methods

Materials

Zinc nitrate hexahydrate (Zn (NO$_3$)$_2$·6H$_2$O, ≥99.99%), 2-methylimidazole (98%), 1,10-phenanthroline monohydrate (Phen, ≥99.99%), ferrous chloride tetrahydrate (FeCl$_2$·4H$_2$O, 98%), ammonium chloride (NH$_4$Cl, 99.5%) ammonium bromide (NH$_4$Br, 99.0%) were sourced from Aladdin.
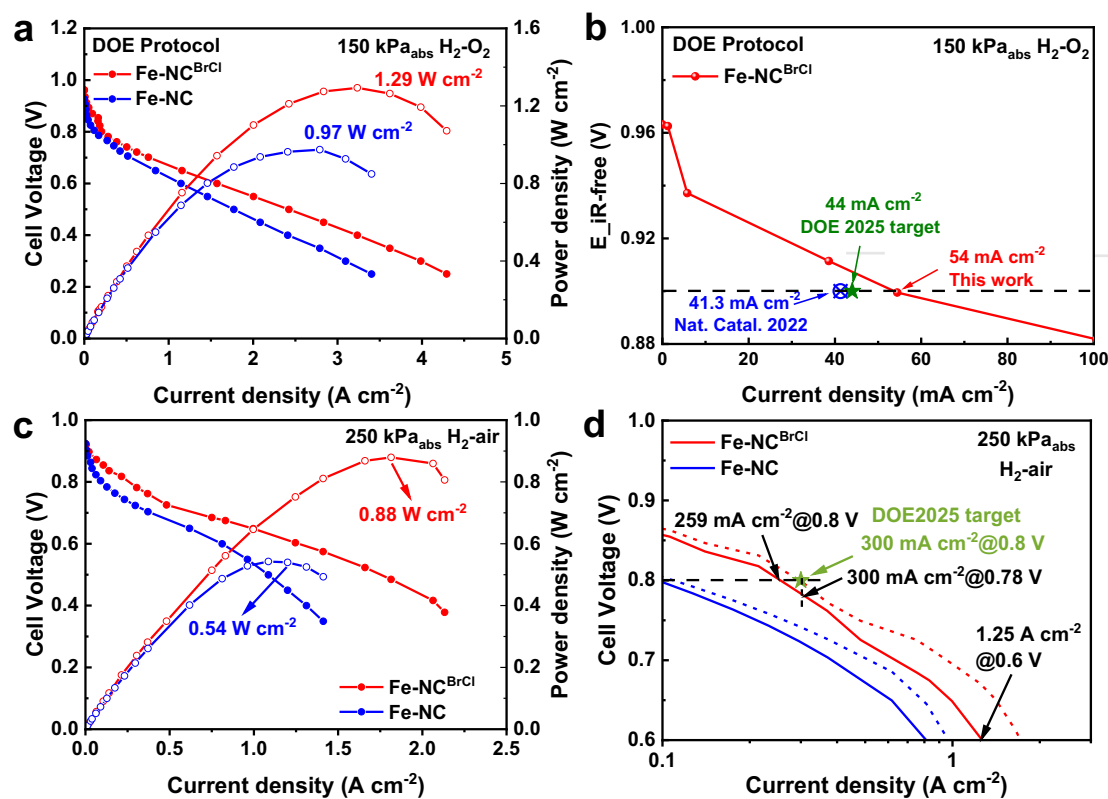
Fig. 4 | The polarization curves obtained by DOE MEA test protocol of PGM-free electrocatalyst. a H_2-O_2 polarization curves, acquired from OCV to 0.70 V in 25 mV steps and 0.70 V to 0.25 V in 50 mV steps, with a hold time of 45 s per point. 0.3 L H_2 min^{-1} and 0.4 L O_2 min^{-1} feed, 100% relative humidity (RH), 150 kPa absolute partial pressure H_2 and O_2, 80 °C. **b** H_2-O_2 polarization curve with iR-correction. **c** H_2-air polarization curves. **d** Tafel plots derived from the ORR polarization curves displayed in (**c**).

Commercial 20 wt% Pt/C (Johnson Matthey) served as a comparison benchmark. 5 wt% Nafion ionomer was purchased from DuPont. GORE-SELECT® membrane (15 μm thickness) was purchased from Sinero Co. Methanol (CH$_3$OH, 99.5%), Isopropanol (C$_3$H$_8$O, 99.5%) were purchased from Chemical Reagent Co., Ltd. Ultrapure water (Millipore, 18.25 MΩ cm) was used throughout all experiments.

Catalyst synthesis

The NC substrate was synthesized through the pyrolysis of a ZIF-8@Phen composite precursor, which included 1,10-phenanthroline monohydrate and ZIF-8 nanocrystals[29]. To prepare the ZIF-8@Phen composite precursors, Zn(NO$_3$)$_2$·6H$_2$O (10 mmol, 2.975 g) and 2-mIm (80 mmol, 6.568 g) were each dissolved separately in 100 mL of methanol using ultrasound for 5 min. The Zn(NO$_3$)$_2$ solution was then rapidly poured into the 2-mIm solution, and the mixture was stirred vigorously for 16 h at room temperature. The resulting white ZIF-8 precipitate was collected by centrifugation, washed several times with methanol, and dried overnight under vacuum at 60 °C. Subsequently, 1.0 g of the obtained ZIF-8 and 0.3 g of 1,10-phenanthroline were dispersed in a 2:1 ethanol and deionized water solution. This mixture was magnetically stirred for 12 h at room temperature and then evaporated in an oil bath at 80 °C. The dry powders were thoroughly ground and pyrolyzed under an Ar flow at 1000 °C (5 °C·min^{-1}) for 1 h, followed by natural cooling to room temperature. The resulting black products were designated as NC.

Next, the NC substrate (100 mg) was ground together with NH$_4$Cl (150 mg), NH4Br (150 mg), and FeCl$_2$·4H$_2$O (6 mg), followed by a heat treatment at 900 °C (10 °C·min^{-1}) under an Ar flow for 1 h to obtain the Fe−NC catalyst, referred to as Fe−NC^{BrCl}. During this process, NH$_4$Cl and NH4Br decomposed to produce NH$_3$, HCl, and HBr gases at high temperatures, generating significant internal stress and etching the carbon. This created numerous mesopores and carbon defects, similar to previously reported Fe-N-C catalysts treated with NH$_3$ gas. In addition, HCl likely dissociated further at high temperatures to form H_2 and Cl_2 gases, where the Cl_2 gas reacted with residual Fe aggregates in the catalysts, facilitating the formation of atomically dispersed Fe sites[53]. For comparison, Fe-NC catalysts were also synthesized without adding NH$_4$Cl or NH$_4$Br, while Fe−NC^{Cl} catalysts were produced with only NH$_4$Cl, and Fe−NC^{Br} catalysts with only NH$_4$Br. ICP-MS analysis revealed Fe contents of 2.25 wt% for Fe−NC and 2.50 wt% for Fe−NC^{BrCl}.

Physical characterization

Scanning electron microscopy (SEM) images were acquired using a Hitachi S4800 at an acceleration voltage of 15 kV. Transmission electron microscopy (TEM) and high-resolution TEM (HR-TEM) analyses were conducted on a TECNAI F20 operating at 200 kV. Scanning transmission electron microscopy (STEM) and elemental mapping were performed with an FEI Talos F200s at 200 kV. High-angle annular dark-field STEM (HAADF-STEM) was carried out on an FEI Themis Z at 200 kV, equipped with a cold field-emission gun and an aberration corrector. For these observations, samples were prepared by depositing ethanol-dispersed samples onto a copper microgrid. Atomic-resolution images were captured with an FEI Titan Themis 60−300 at 200 kV. Nitrogen physisorption measurements were conducted using a Micromeritics Tristar 3020 Surface Area Analyzer after drying the samples under vacuum at 200 °C for 3 h. X-ray powder diffraction (XRD) patterns were obtained using a Rigaku SmartLab-SE Powder X-ray diffractometer with Cu-Kα radiation (λ = 1.5406 Å), scanned at a rate of 10° min^{-1} over a 2θ range of 10−90°. X-ray photoelectron
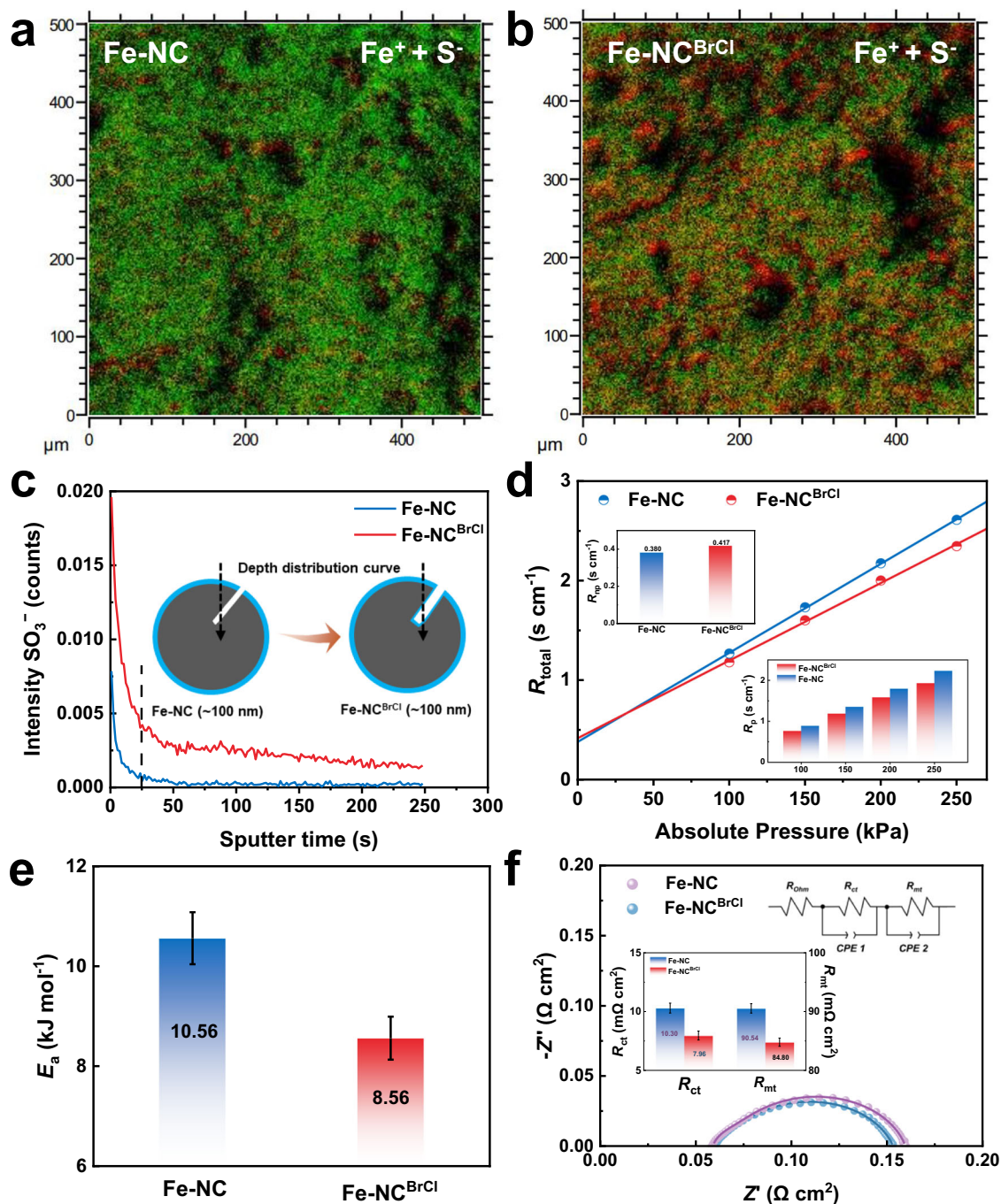
Fig. 5 | The interface effect of MEA. a, b The secondary ion two-dimensional imaging from ToF-SIMS, **a** Fe–NC, **b** Fe–NC^{BrCl}. The green is S$^-$, the red is Fe$^+$. **c** Integral SO$_3^-$ distribution in cathode catalyst layer shows intensity gradients from both Fe–NC (blue) and Fe–NC^{BrCl} (red) catalysts. **d** Relationship between R_{total} and absolute gas pressure obtained by the limiting current method. Insets were R_{np} and R_p. **e** An Arrhenius plot of i_0 obtained from the Nyquist plots shown in Supplementary Fig. 37. **f** Nyquist plots for PEMFCs of indicated cathode catalysts at the current density of 1.0 A cm^{-2}, the inset shows the equivalent circuit model, R_{ct} and R_{mt} of Fe–NC and Fe–NC^{BrCl} obtained by EIS fitting. Error bars represent the standard deviation of the fitting results.

spectroscopy (XPS) was performed on a PHI Quantum-2000 using Al Kα radiation (1486.6 eV), with binding energies referenced to C 1s at 284.8 eV. The iron concentration in the samples was determined using inductively coupled plasma mass spectrometry (ICP-MS) on a Perkin Elmer NexION 300. Fe K-edge X-ray absorption spectra (XAS) were collected in fluorescence mode at beamline 1W1B of the Beijing Synchrotron Radiation Facility (BSRF). N K-edge XAS spectra were acquired at the TPS 44 A station of the National Synchrotron Radiation Research Center (NSRRC) in Hsinchu, Taiwan.

Electrochemical measurements

At room temperature, all electrochemical curves were conducted using a three-electrode setup with a Pine on a CHI 760E electrochemical workstation. The reference and counter electrodes were a saturated calomel electrode (KCl-saturated) and a graphite rod, respectively. To prepare a uniform catalyst ink, 6 mg of catalyst was sonicated for 30 min in 1 mL of a mixture containing 600 μL isopropanol, 380 μL ultrapure water, and 20 μL of 5 wt% Nafion solution. For the commercial 20 wt% Pt/C sample, 1 mg of catalyst was dispersed

in 1 mL of a 0.05 wt% Nafion solution. A specific volume of the catalyst ink was applied to the polished glassy carbon rotating ring-disk electrode (RRDE, diameter 5.61 mm, area 0.2475 cm^2) to achieve the desired catalyst loading. For all ORR experiments, a glassy carbon RRDE coated with PGM-free catalyst ink was used as the working electrode, with a loading of 0.6 mg cm^{-2} at 900 r.p.m. in 0.1 M H$_2$SO$_4$ electrolyte and the measurements are conducted at 30 °C. A commercial 20 wt% Pt/C catalyst served as a reference, tested in 0.1 M HClO$_4$ with a charge of 15 μg$_{Pt}$ cm^{-2}. The reference electrode was calibrated to a reversible hydrogen electrode (RHE) in the same electrolyte before each test. ORR polarization curves for PGM-free catalysts were obtained using linear sweep voltammetry (LSV) from 0.1 to 1.1 V (*vs.* RHE) at 900 r.p.m. with a scan rate of 10 mV s^{-1}. The resistance is automatically compensated by 80%, and the resistance in the impedance spectrum mode is measured by the pine system. The electrolyte was measured by pH instruments to ensure a constant test environment (pH = 0.7 for 0.1 M H$_2$SO$_4$). All potentials were converted to RHE potentials using the equation:

$$E_{RHE} = E_{SCE} + 0.2415 + 0.059 \times pH - IR_S \tag{2}$$

Quantification of site density and turnover frequency by nitrite stripping

The SD was determined using the nitrite reduction method by Kucernak[37]. Briefly, nitrite interacts with the Fe metal center to form stable poisoned adducts, which can be fully stripped within the potential range of 0.35 to −0.35 V (*vs.* RHE). The excess coulometric charge (Q_{strip}) from the stripping peak is proportional to the SD:

$$SD\ (\text{sites}\,g^{-1}) = \frac{Q_{strip}\,(C\,g^{-1}) \times N_A\,(\text{sites}\,mol^{-1})}{n_{strip}F\,(C\,mol^{-1})} \tag{3}$$

$$TOF\ (s^{-1}) = \frac{\Delta j_m\,(A\,g^{-1}) \times N_A\,(\text{sites}\,mol^{-1})}{SD\,(\text{sites}\,g^{-1}) \times F\,(C\,mol^{-1})} \tag{4}$$

where n_{strip} (=5) is the number of transferred electrons per stripped one nitrite. N_A is Avogadro constant (6.02×10^{23} sites mol^{-1}). F is Faraday's constant (96485 C mol^{-1}). Δj_m is the disparity in mass activity of the catalyst at 0.8 V or 0.85 V.

Fuel cell MEA tests

Membrane electrode assembly (MEA): To prepare the cathode ink, Fe–NC catalysts were ultrasonically blended with 0.2 mL of deionized water, 0.8 mL of isopropanol, and a 5 wt% Nafion solution in an ice bath for 1 h[29]. The ink was applied to a gas diffusion layer (GDL) made from PTFE-treated Toray 060 carbon paper, achieving a catalyst loading of 3.5 mg cm^{-2}. The cathode catalyst layer contained about 50 wt% Nafion. The anode catalyst consisted of 40 wt% Pt/C, with a platinum loading of 0.4 mg$_{Pt}$ cm^{-2}. The MEA assembly involved hot-pressing the fabricated cathode with an anode, a 15-μm-thick GORE-SELECT® membrane, and a gasket at 130 °C and a pressure of 3 MPa for 90 s. The MEA had an active area of 1.1 × 1.1 cm^2.

MEA test: A Model 850e fuel cell test system (Scribner Associates, Inc.) was utilized to obtain polarization curves at 80 °C. Initially, the cell was brought to 80 °C without any flow, followed by passing humidified N$_2$ at 0.3 L min^{-1} over both the cathode and anode for 1 h to ensure membrane and ionomer hydration. The cathode received air/oxygen at flow rates of 1.0/0.4 L min^{-1}, while the anode was supplied with H$_2$ at a flow rate of 0.3 L min^{-1}. During the fuel cell tests, reactant gases were subjected to absolute pressures of either 150 kPa or 250 kPa. Throughout the polarization curve measurements, the dew points of the cathode and anode gases, as well as the cell temperature, were kept constant at 80 °C. MEA performance measurements under H$_2$–O$_2$

and H$_2$–air conditions adhered to protocols recommended by the US ElectroCat Consortium[27]. Specifically, a 45-s holding time at each voltage was implemented to attain a steady-state current density. Electrochemical impedance spectroscopy was performed at a steady current of 1.0 A cm^{-2}, spanning a frequency range from 10 kHz to 0.1 Hz with an AC amplitude constituting 10% of the DC current.

PEMFCs stack test: A PEMFCs stack is made up of three MEAs (each active area is 25 cm^2, cathode catalyst loading is 2.0 mg cm^{-2}) connected in a series. O$_2$ flowing at 1.0 L min^{-1} and H$_2$ flowing at 0.8 L min^{-1} were supplied to the cathode and anode, respectively. The cathode and anode gas dew points and the cell temperature were maintained at 70 °C and the absolute pressures were 50 kPa for reactant gases (background pressure is 0 kPa) during the measurement of the polarization curves.

Computational details

All spin-polarized calculations were performed with the VASP[54]. The projector augmented wave method and the PBE functional of generalized gradient approximation (GGA) with were applied[55,56]. The Van der Waals interaction was included in this study[57]. The kinetic cut-off energy for the planewave basis was 400 eV. The vacuum layer between the periodic images of Fe–N$_4$–C sheets was 20 Å. For the geometry optimization, the Brillouin zone was sampled with a 4 × 4 × 1 k-point mesh of the Monkhorst–Pack scheme, and all atoms in the supercell are allowed to relax. The energy convergence criterion is 10^{-5} eV, and the final forces on all atoms are less than 0.01 eV Å^{-1}. The GGA + U method is applied to account for the strongly localized d orbitals of the Fe[58]. The Hubbard U values for the Fe atom of the Fe–N$_4$ structure are chosen to be 3.3, attempting to have a brief insight into the intermediate adsorption at the Fe atom during O$_2$ reduction. The first carbon shell of the Fe–N$_4$ center was doped with the chlorine or bromine atom, respectively, forming the relevant Fe–N$_4$–Cl and Fe–N$_4$–Br structures.

Data availability

The data that support the findings of this study are available within the article and its Supplementary Information files. All other relevant data supporting the findings of this study are available from the corresponding authors upon request. Source data file has been deposited in Figshare, https://doi.org/10.6084/m9.figshare.25701651.

References

1. Kodama, K. et al. Challenges in applying highly active Pt-based nanostructured catalysts for oxygen reduction reactions to fuel cell vehicles. *Nat. Nanotechnol.* **16**, 140–147 (2021).
2. Sui, S. et al. A comprehensive review of Pt electrocatalysts for the oxygen reduction reaction: Nanostructure, activity, mechanism and carbon support in PEM fuel cells. *J. Mater. Chem. A* **5**, 1808–1825 (2017).
3. Kulkarni, A. et al. Understanding catalytic activity trends in the oxygen reduction reaction. *Chem. Rev.* **118**, 2302–2312 (2018).
4. Yang, C. et al. Sulfur-anchoring synthesis of platinum intermetallic nanoparticle catalysts for fuel cells. *Science* **374**, 459–464 (2021).
5. Chong, L. et al. Ultralow-loading platinum-cobalt fuel cell catalysts derived from imidazolate frameworks. *Science* **362**, 1276–1281 (2018).
6. Chen, F. et al. Blocking the sulfonate group in Nafion to unlock platinum's activity in membrane electrode assemblies. *Nat. Catal.* **6**, 392–401 (2023).
7. Zhan, C. et al. Zinc intercalated lattice expansion of ultrafine platinum–nickel oxygen reduction catalyst for PEMFC. *Adv. Funct. Mater.* **33**, 2212442 (2022).
8. Huang, L. et al. Progress of Pt-based catalysts in proton-exchange membrane fuel cells: a review. *J. Electrochem.* **28**, 2108061 (2022).
9. Zhao, Z. et al. Graphene-nanopocket-encaged PtCo nanocatalysts for highly durable fuel cell operation under demanding ultralow-Pt-loading conditions. *Nat. Nanotechnol.* **17**, 968–975 (2022).

10. Xiao, F. et al. Atomically dispersed Pt and Fe sites and Pt–Fe nanoparticles for durable proton exchange membrane fuel cells. *Nat. Catal.* **5**, 503–512 (2022).

11. Zhao, Z. et al. Pt-based nanocrystal for electrocatalytic oxygen reduction. *Adv. Mater.* **31**, 1808115 (2019).

12. Zhang, T. et al. Adjusting the alloying degree of Pt_3Zn to improve acid oxygen reduction activity and stability. *J. Electrochem* **28**, 2106091 (2022).

13. Jaouen, F. et al. Heat-treated Fe/N/C catalysts for O_2 electro-reduction: are active sites hosted in micropores? *J. Phys. Chem. B* **110**, 5553–5558 (2006).

14. Thompson, S. T. et al. ElectroCat: DOE's approach to PGM-free catalyst and electrode R&D. *Solid State Ion.* **319**, 68–76 (2018).

15. Cheng, X. et al. Nano-geometric deformation synergistic Co nano-particles & Co-N_4 composite site for proton exchange membrane fuel cells. *Energy Environ. Sci.* **14**, 5958–5967 (2021).

16. Yin, S. et al. Self-template synthesis of atomically dispersed Fe/N-codoped nanocarbon as efficient bifunctional alkaline oxygen electrocatalyst. *ACS Appl. Energy Mater.* **3**, 625–634 (2020).

17. Lin, X. et al. Large-scale production of holey carbon nanosheets implanted with atomically dispersed Fe sites for boosting oxygen reduction electrocatalysis. *Nano Res.* **15**, 1926–1933 (2021).

18. Qu, X. et al. In-situ growth of carbon nanotubes for improving the performance of Co-N/C catalysts in proton exchange membrane fuel cell. *Chem. Eng. J.* **461**, 142054 (2023).

19. Yin, S. et al. Construction of highly active metal-containing nano-particles and FeCo-N_4 composite sites for the acidic oxygen reduction reaction. *Angew. Chem. Int Ed.* **59**, 21976–21979 (2020).

20. Li, C. et al. Fe nanoparticles encapsulated in N-doped porous car-bon for efficient oxygen reduction in alkaline media. *J. Electrochem.* **29**, 2210241 (2023).

21. Li, Y. et al. Recent advances in exploring highly active & durable PGM-free oxygen reduction catalysts. *J. Electrochem.* **29**, 2215002 (2023).

22. Zitolo, A. et al. Identification of catalytic sites for oxygen reduction in iron- and nitrogen-doped graphene materials. *Nat. Mater.* **14**, 937 (2015).

23. Strickland, K. et al. Highly active oxygen reduction non-platinum group metal electrocatalyst without direct metal–nitrogen coordi-nation. *Nat. Commun.* **6**, 7343 (2015).

24. He, Y. et al. Atomically dispersed metal–nitrogen–carbon catalysts for fuel cells: advances in catalyst design, electrode performance, and durability improvement. *Chem. Soc. Rev.* **49**, 3484–3524 (2020).

25. Zhang, H. et al. High-performance fuel cell cathodes exclusively containing atomically dispersed iron active sites. *Energy Environ. Sci.* **12**, 2548–2558 (2019).

26. Jiao, L. et al. Chemical vapour deposition of Fe–N–C oxygen reduction catalysts with full utilization of dense Fe–N_4 sites. *Nat. Mater.* **20**, 1385–1391 (2021).

27. Liu, S. et al. Atomically dispersed iron sites with a nitrogen–carbon coating as highly active and durable oxygen reduction catalysts for fuel cells. *Nat. Energy* **7**, 652–663 (2022).

28. Mehmood, A. et al. High loading of single atomic iron sites in Fe–NC oxygen reduction catalysts for proton exchange membrane fuel cells. *Nat. Catal.* **5**, 311–323 (2022).

29. Yin, S. et al. Seizing gaseous Fe^{2+} to densify O_2-accessible Fe-N_4 sites for high-performance proton exchange membrane fuel cells. *Energy Environ. Sci.* **15**, 3033–3040 (2022).

30. Cheng, X. et al. Instantaneous free radical scavenging by CeO_2 nanoparticles adjacent to the Fe-N_4 active sites for durable fuel cells. *Angew. Chem. Int Ed.* **62**, e202306166 (2023).

31. Cheng, X. et al. Revealing the optimal configuration for synergy effect of metal nanoparticles and MN_4 sites for oxygen reduction reaction. *Nano Energy* **100**, 107440 (2022).

32. Wan, X. et al. Fe–N–C electrocatalyst with dense active sites and efficient mass transport for high-performance proton exchange membrane fuel cells. *Nat. Catal.* **2**, 259–268 (2019).

33. Li, J. et al. Evolution pathway from iron compounds to Fe1(II)–N_4 sites through gas-phase iron during pyrolysis. *J. Am. Chem. Soc.* **142**, 1417–1423 (2019).

34. Jin, Z. et al. Understanding the inter-site distance effect in single-atom catalysts for oxygen electroreduction. *Nat. Catal.* **4**, 615–622 (2021).

35. Hai, X. et al. Scalable two-step annealing method for preparing ultra-high-density single-atom catalyst libraries. *Nat. Nanotechnol.* **17**, 174–181 (2021).

36. Li, Q. et al. Highly efficient Fe-N-C oxygen reduction electrocatalyst engineered by sintering atmosphere. *J. Power Sources* **449**, 227497 (2020).

37. Malko, D. et al. In situ electrochemical quantification of active sites in Fe–N/C non-precious metal catalysts. *Nat. Commun.* **7**, 13285 (2016).

38. Wang, L. et al. Phosphorus and halogen co-doped graphene materials and their electrochemistry. *Chem. Eur. J.* **22**, 15444–15450 (2016).

39. Proietti, E. et al. Iron-based cathode catalyst with enhanced power density in polymer electrolyte membrane fuel cells. *Nat. Commun.* **2**, 416 (2011).

40. Wang, Y. et al. S-Doping of an Fe/N/C ORR catalyst for polymer electrolyte membrane fuel cells with high power density. *Angew. Chem. Int Ed.* **127**, 10045–10048 (2015).

41. Fu, X. et al. In situ polymer graphenization ingrained with nano-porosity in a nitrogenous electrocatalyst boosting the performance of polymer-electrolyte-membrane fuel cells. *Adv. Mater.* **29**, 1604456 (2017).

42. Liu, Q. et al. The solid-phase synthesis of an Fe-N-C electrocatalyst for high-power proton-exchange membrane fuel cells. *Angew. Chem. Int Ed.* **57**, 1204–1208 (2018).

43. Li, Y. et al. A general carboxylate-assisted approach to boost the ORR performance of ZIF-derived Fe/N/C catalysts for proton exchange membrane fuel cells. *Adv. Funct. Mater.* **31**, 2009645 (2021).

44. Men, S. et al. X-ray photoelectron spectroscopy of pyridinium-based ionic liquids: comparison to imidazolium- and pyrrolidinium-based analogues. *ChemPhysChem* **16**, 2211–2218 (2015).

45. Rauf, M. et al. Insight into the different ORR catalytic activity of Fe/N/C between acidic and alkaline media: Protonation of pyridinic nitrogen. *Electrochem. Commun.* **73**, 71–74 (2016).

46. Daniel, R. et al. Measurement of oxygen transport resistance in PEM fuel cells by limiting current methods. *J. Electrochem. Soc.* **156**, B991–B1003 (2009).

47. Ohma, A. et al. Analysis of proton exchange membrane fuel cell catalyst layers for reduction of platinum loading at Nissan. *Electrochim. Acta* **56**, 10832–10841 (2011).

48. Huang, J. et al. Review of characterization and modeling of polymer electrolyte fuel cell catalyst layer: The blessing and curse of iono-mer. *Front Energy* **11**, 334–364 (2017).

49. Dang, D. et al. High-performance, ultralow platinum membrane electrode assembly fabricated by in situ deposition of a Pt shell layer on carbon-supported Pd nanoparticles in the catalyst layer using a facile pulse electrodeposition approach. *ACS Catal.* **5**, 4318–4324 (2015).

50. Ono, Y. et al. Influence of equivalent weight of ionomer on local oxygen transport resistance in cathode catalyst layers. *J. Electrochem Soc.* **160**, F779–F787 (2013).

51. Kongkanand, A. et al. The priority and challenge of high-power performance of low-platinum proton-exchange membrane fuel cells. *J. Phys. Chem. Lett.* **7**, 1127–1137 (2016).

52. Takahashi, M. et al. Reaction behavior of $LiFePO_4$ as a cathode material for rechargeable lithium batteries. *Solid State Ion.* **148**, 283–289 (2002).

53. Varnell, J. A. et al. Identification of carbon-encapsulated iron nanoparticles as active species in non-precious metal oxygen reduction catalysts. *Nat. Commun.* **7**, 12582 (2016).
54. Kresse, G. et al. Ab initio molecular dynamics for liquid metals. *Phys. Rev. B* **47**, 558–561 (1993).
55. Kresse, G. et al. From ultrasoft pseudopotentials to the projector augmented-wave method. *Phys. Rev. B* **59**, 1999 (1758).
56. Perdew, J. et al. Generalized gradient approximation made simple. *Phys. Rev. Lett.* **78**, 1396 (1997).
57. Grimme, S. et al. Effect of the damping function in dispersion corrected density functional theory. *J. Comput. Chem.* **32**, 1456–1465 (2011).
58. Dudarev, S. L. et al. Electron-energy-loss spectra and the structural stability of nickel oxide: an LSDA+U study. *Phys. Rev. B* **57**, 1505 (1998).

Author contributions
The project was conceptualized by S.Y., R.H., Y.J., and S.S. R.H., Y.J., and S.S. supervised this project. S.Y. and L.C. synthesized the catalysts, conducted the electrochemical tests, and the related data processing. S.Y. performed materials characterization with the help of X.C., H.Z., and Y.H. H.H. performed the Fe K-edge XAS characterization. X.K. and Y.L. performed the N K-edge XANES. Y.J. and S.Y. performed the theoretical calculations and mechanistic analysis. R.H. and S.S. provided suggestions on the work. S.Y. and R.H. wrote the manuscript; and L.C., J.Y., R.H., Y.J., and S.S. helped with the revision of the manuscript. We appreciate the Beijing Synchrotron Radiation Facility (1W1B, BSRF) and the National Synchrotron Radiation Research Center (NSRRC) in Hsinchu, Taiwan, R.O.C. for help with XAS characterizations. All authors discussed the results.

Competing interests
The authors declare no competing interests.

Additional information
Supplementary information The online version contains supplementary material available at https://doi.org/10.1038/s41467-024-51858-w.

Correspondence and requests for materials should be addressed to Rui Huang, Yanxia Jiang or Shigang Sun.

Peer review information *Nature Communications* thanks Jian Xie, and the other, anonymous, reviewer(s) for their contribution to the peer review of this work. A peer review file is available.

Reprints and permissions information is available at http://www.nature.com/reprints

Publisher's note Springer Nature remains neutral with regard to jurisdictional claims in published maps and institutional affiliations.